Supporting information

Engineering O-O formation on dual-atom Fe-Mo catalysts for oxygen electrocatalysis

Luoluo Qi[a], Yanan Tang[b,*], Tao Gan[c,*], Jingqi Guan[a,*]

[a] Institute of Physical Chemistry, College of Chemistry, Jilin University, 2519 Jiefang Road, Changchun 130021, P. R. China. *E-mail: guanjq@jlu.edu.cn (J.Q. Guan)

[b] College of Physics and Electronic Engineering, Zhengzhou Normal University, Zhengzhou 450044, China. *E-mail: yntang2010@163.com (Y.N. Tang)

[c] Shanghai Synchrotron Radiation Facility, Shanghai Advanced Research Institute, Chinese Academy of Sciences, Shanghai, 201204, China. E-mail: gant@sari.ac.cn (T. Gan)

Material characterization

X-ray powder diffraction for FeMo/NC and control catalysts was available from the Shimadzu 6000. Surface micromorphology and elemental distribution of FeMo/NC were monitored by JEM-2100 aberration-corrected transmission electron microscope and Talos F200s G2. The surface chemical state and elemental composition of FeMo/NC and Fe/NC were characterized by Thermo ESCALAB 250 X-ray photoelectron spectrometer. The X-ray absorption fine structure (XAFS) spectra at the Fe K-edge and Mo K-edge were recorded at the BL11B beamline of Shanghai Synchrotron Radiation Facility (SSRF).

Electrochemical evaluation

The ORR/OER properties of different materials in alkaline electrolytes were examined on a CHI 760E electrochemical workstation with a standard three-electrode system. In ORR, the three-electrode system involves glassy-carbon coated with the catalyst (WE), Pt electrode (CE) and saturated calomel electrode (RE). Firstly, cyclic voltammetry (CV) tests were conducted in O_2/N_2-saturated 0.1 M KOH media to bring the catalyst to a steady state. Then, linear sweep voltammetry (LSV) tests were performed using the rotating disk electrode (RDE) system in O_2/N_2-saturated 0.1 M KOH at different speeds (400-2025 rpm) to determine the ORR performance. Additionally, LSV tests were conducted using the rotating ring-disk electrode (RRDE) system at 1600 rpm to evaluate the ORR performance. Lastly, the tolerance (methanol, CO and KSCN) and durability of FeMo/NC were evaluated in O_2-saturated 0.1 M KOH medium (1600 rpm). For the OER, the three-electrode system consists of a graphite plate loaded with the catalyst (WE), a platinum sheet (CE) and SCE (RE). First, the catalyst was brought to a steady state using electrochemical CV testing. Then, the OER performance was examined by LSV measurement. Finally, the long-term stability of the catalyst was evaluated by chronoamperometry. Test potentials in all experimental curves were transformed according to $E_{RHE} = E_{SCE} + 0.241 + 0.059 \times pH$, with pH = 13 in ORR and pH = 14 in OER.

Zn-air battery test

The performance of the assembled rechargeable and flexible zinc-air batteries was estimated by the CT3002A LANHE battery test system. In this case, the air cathode and

anode were modified carbon paper coated with the catalyst and zinc plate, respectively, and a mixture of 6 M KOH and 0.2 M $Zn(OAc)_2$ or PVA gel containing KOH and $Zn(OAc)_2$ was used as the electrolyte. The CHI 760E electrochemical workstation measured open circuit voltage (OCV) and discharge polarization curves. The CT3002A LANHE battery test system tested voltage plateaus at different current densities, specific capacity and charge/discharge cycle stability.

DFT methods

All the density functional theory (DFT) calculations were carried out using Vienna ab initio simulation package (VASP), and the spin polarization effect was considered[1]. The projector–augmented wave (PAW) method was adopted to describe the interaction between valence electrons and ionic cores[2], while the exchange–correlation effect treated using the Perdew–Burke–Ernzerhof (PBE) functional within the generalized gradient approximation (GGA)[3]. The van der Waals effects were accounted for using the DFT–D3 correction scheme[4]. Aplane–wave basis set with a cutoff energy of 400 eV was applied. The convergence criteria were set to 10^{-4} eV for the total energy and 0.03 eV/Å for the Hellmann–Feynman forces. To study the ORR and OER mechanisms, a rectangular graphene supercell was built, with both surface lattice constants larger than 17 Å to ensure sufficient separation. A vacuum layer of 15 Å was added along the *z*–direction to eliminate interlayer interactions. For such supercell, a Monkhorst–Pack *k*–point mesh of 2×2×1 was used for structural relaxation, and a denser 5×5×1 grid was employed for the calculation of densities of states (DOS)[5].

The computational hydrogen electrode (CHE) model was adopted to study the reaction

thermodynamics of ORR and OER[6]. The reaction free energy for each elementary step was calculated following $\Delta G = \Delta E + \Delta E_{ZPE} - T\Delta S$. Here, ΔE is the calculated reaction energy from DFT total energies, ΔE_{ZPE} is the zero–point energy correction, and $T\Delta S$ (with $T = 298.15$ K) represents the entropic contribution. ΔE_{ZPE} and $T\Delta S$ for the adsorbed intermediates and the free molecules were derived from vibrational frequency calculations and the NIST database, respectively[7]. Solvation effects were accounted for using the VASPsol implicit solvation model[8]. Herein, the electrode potential effect was included by optimizing both the coordinates and electron numbers of the systems at the desired applied potential vs. standard hydrogen electrode (SHE)[9, 10]. The relationship between the electrode potentials versus SHE and the reversible hydrogen electrode (RHE) was established by: $eU_{RHE} = eU_{SHE} + k_B T \times pH \times \ln 10$[11].

According to the experimental results, we considered alkaline conditions (pH = 13 for ORR and pH = 14 for OER). The 4–electron ORR pathway proceeds as follows[12]:

$$* + O_2(g) + H_2O(l) + e^- \rightarrow *OOH + OH^- \quad (1)$$

$$*OOH + e^- \rightarrow *O + OH^- \quad (2)$$

$$*O + H_2O(l) + e^- \rightarrow *OH + OH^- \quad (3)$$

$$*OH + e^- \rightarrow OH^- + * \quad (4)$$

The reaction free energy of the above four elementary steps at electrode potential U_{RHE} can be calculated by:

$$\Delta G_a = \Delta G_{*OOH} - 4.92 + eU_{RHE} \quad (5)$$

$$\Delta G_b = \Delta G_{*O} - \Delta G_{*OOH} + eU_{RHE} \quad (6)$$

$$\Delta G_c = \Delta G_{*OH} - \Delta G_{*O} + eU_{RHE} \quad (7)$$

$$\Delta G_d = -\Delta G_{*OH} + eU_{RHE} \quad (8)$$

Here, ΔG_{*OOH}, ΔG_{*O}, and ΔG_{*OH} denote the adsorption free energies of *OOH, *O, and *OH, respectively, and are calculated by referring to the free energy of H_2O and H_2:

$$\Delta G_{*OOH} = G_{*OOH} - (2G_{H2O} - 3/2G_{H2}) - G_{*} \quad (9)$$

$$\Delta G_{*O} = G_{*O} - (G_{H2O} - G_{H2}) - G_{*} \quad (10)$$

$$\Delta G_{*OH} = G_{*OH} - (G_{H2O} - 1/2G_{H2}) - G_{*} \quad (11)$$

Note the OER can be considered as the reverse reaction of the ORR. Moreover, under electrochemical operating conditions, the catalyst's active sites are often pre-covered by *OH and *O species formed during water oxidation. This pre-adsorption is explicitly incorporated within the CHE formalism[13, 14].

Kinetic current density (j_k)

The kinetic current density (j_k), represents the intrinsic activity of the catalyst, which reflects the intrinsic reaction rate per unit area of the catalyst surface after excluding mass transfer limitations such as oxygen diffusion.

$$\frac{1}{j} = \frac{1}{j_k} + \frac{1}{j_L} \quad (12)$$

Where j is the experimentally measured total current density, j_L is the diffusion-limited current density.

The electron transfer number (n)

The electron transfer number (n) can be estimated in conjunction with the RDE tests at different rotational speeds (400-2025 rpm) based on the Koutechy-Levich (K-L) equation[15].

$$\frac{1}{j} = \frac{1}{j_k} + \frac{1}{B\omega^{1/2}} \quad (13)$$

$$B = 0.62nFC_0v^{-1/6}D_0^{2/3} \quad (14)$$

In the formula, j and j_k respectively represent the measured and kinetic current densities (mA cm^{-2}). ω refers to the angular velocity. n is the electron transfer number of the ORR. F is the faraday constant (96500 C mol^{-1}). C_0 and D_0 are the bulk concentration (1.2×10^{-3} mol L^{-1}) and diffusion coefficient (1.9×10^{-5} cm^2 s^{-1}) of O_2 in 0.1 M KOH. v is the dynamic viscosity (0.01 cm^2 s^{-1}).

H_2O_2 yield (%) and electron transfer number (n)

The H_2O_2 yield and n can be calculated form the data collected from the RRDE test using the following equation, thereby determining the two-electron or four-electron transfer ORR pathway[16].

$$H_2O_2(\%) = 200 \times \frac{I_r/N}{I_d + I_r/N} \quad (15)$$

$$n = 4 \times \frac{I_d}{I_d + I_r/N} \quad (16)$$

In which, I_d and I_r represent the disk current and the ring current, respectively. N refers to the collection efficiency of the ring electrode, with a specific value of 0.25.

Power density

The power density can be used to evaluate the ability of a battery to provide electrical energy[17].

$$P = U \times I \quad (17)$$

In this equation, P refers to the power density (mW cm^{-2}), U is the discharge voltage (V), I is the discharge current density (mA cm^{-2}).

Specific capacity

The specific capacitance can be used to measure the efficiency of a battery by the amount of electricity released per unit time of the battery[18].

$$Specific\ capacity\ (mA\ h\ gZn^{-1}) = \frac{discharge\ current\ \times time}{Mass\ of\ Zn\ plate\ consumed} \quad (18)$$

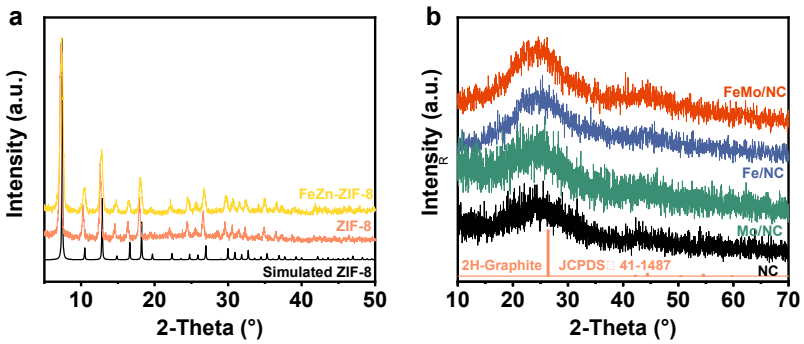

Fig. S1. XRD patterns of (a) simulated ZIF-8, ZIF-8, FeZn-ZIF-8, and (b) 2H-Graphite, NC, Mo/NC, Fe/NC and FeMo/NC.

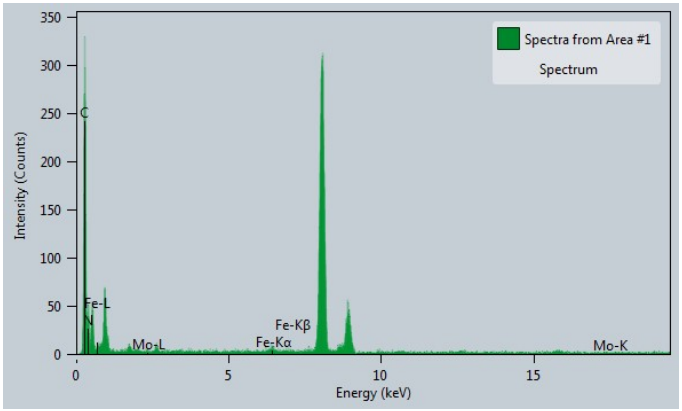

Fig. S2. EDS mapping image of FeMo/NC.

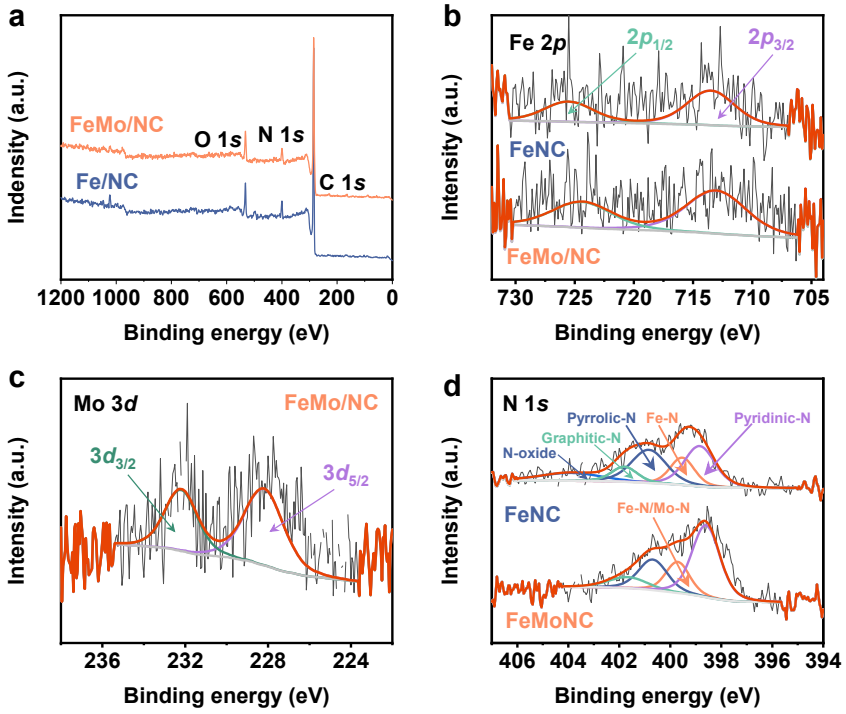

Fig. S3. (a) Full range XPS survey spectrum of FeMo/NC and Fe/NC. (b) High-resolution XPS spectrum of (b) Fe 2*p* for FeMo/NC and Fe/NC, (c) Mo 3*d* for FeMo/NC and (d) N 1*s* for FeMo/NC and Fe/NC.

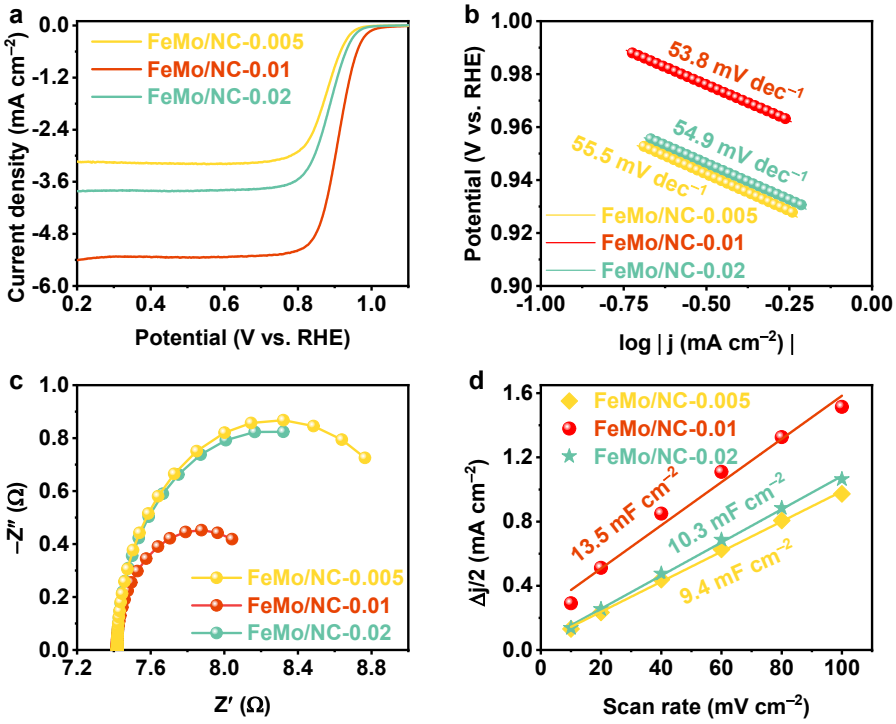

Fig. S4. The ORR performance of FeMo/NC-x (x = 0.005, 0.01 and 0.02) in 0.1 M KOH. (a) LSV curves, (b) Tafel slopes, (c) Nyquist plots and (d) Double-layer capacitance (C_{dl}).

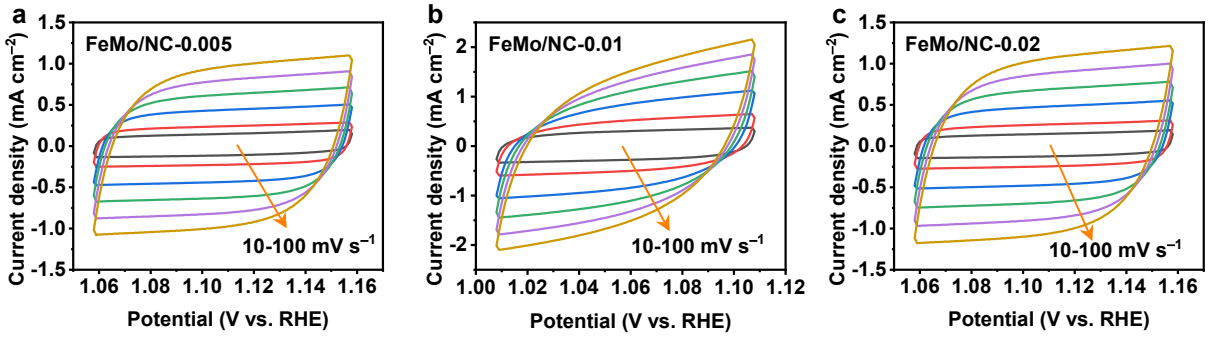

Fig. S5. Cyclic voltammograms (CV) at 10-100 mV s^{-1} in non-Faradaic potential window of (a) FeMo/NC-0.005, (b) FeMo/NC-0.01 and (c) FeMo/NC-0.02.

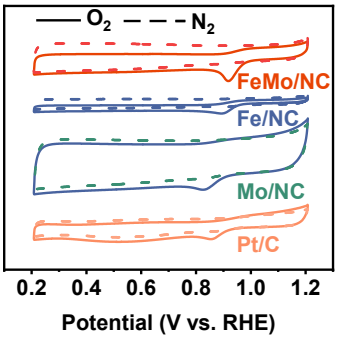

Fig. S6. CV curves of FeMo/NC, Fe/NC, Mo/NC and Pt/C in O_2 and N_2-saturated 0.1 M KOH solution.

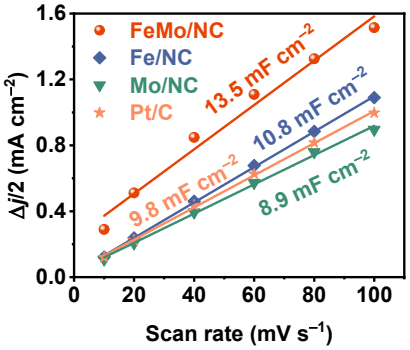

Fig. S7. Electrochemical double-layer capacitance of FeMo/NC, FE/NC, Mo/NC and Pt/C.

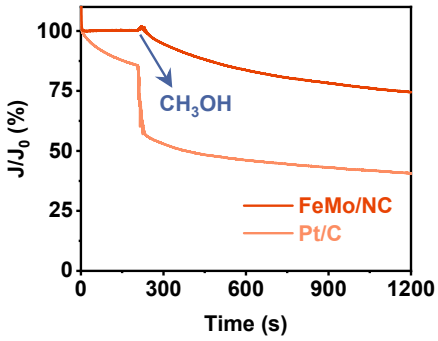

Fig. S8. Fuel crossover effect test of FeMo/NC and Pt/C.

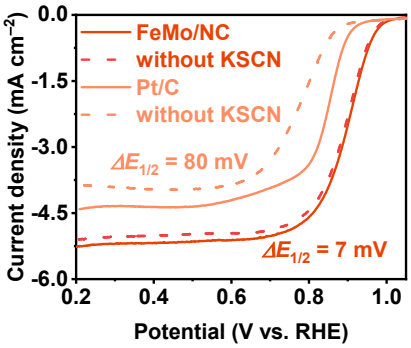

Fig. S9. LSV polarization curves without and with 10 mM KSCN of FeMo/NC and Pt/C.

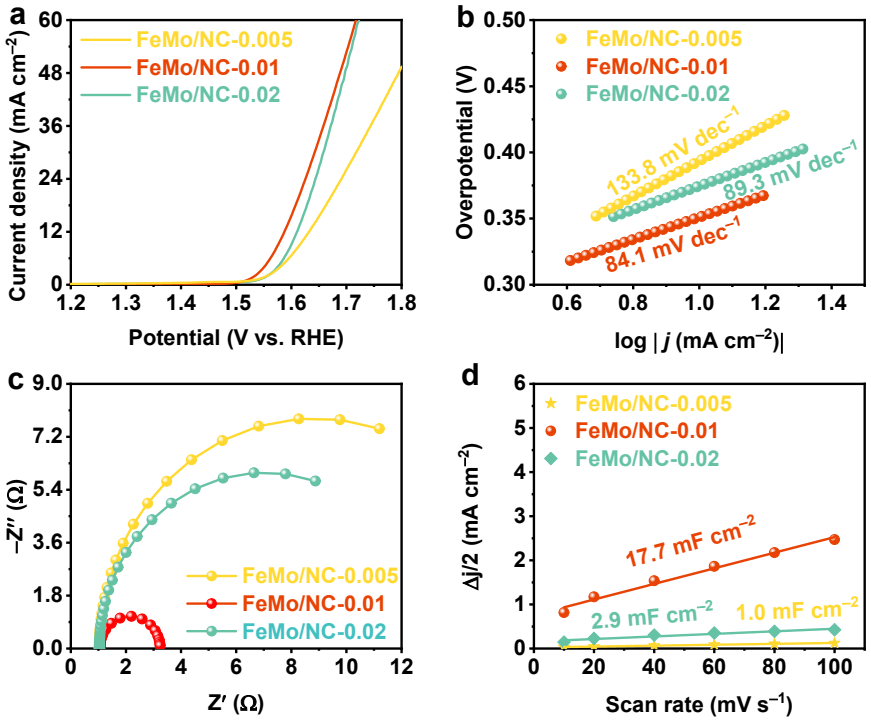

Fig. S10. The OER performance of FeMo/NC-x (x = 0.005, 0.01 and 0.02) in 1.0 M KOH. (a) LSV curves, (b) Tafel slopes, (c) Nyquist plots and (d) Double-layer capacitance (C_{dl}).

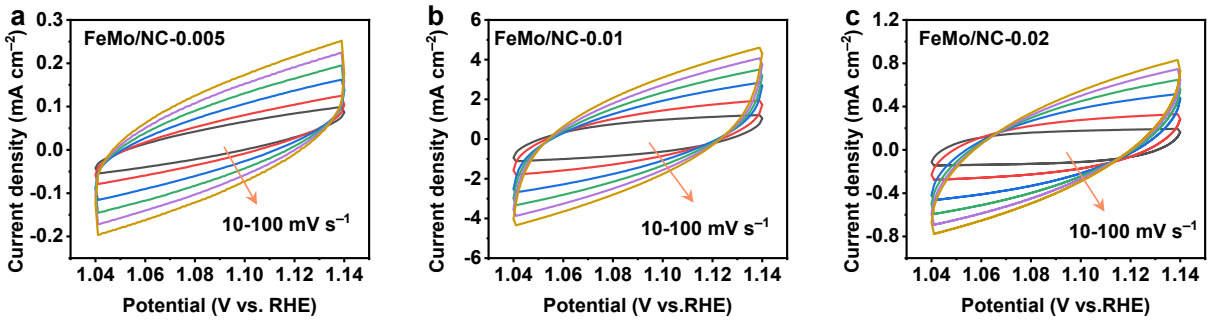

Fig. S11. Cyclic voltammograms (CV) at 10-100 mV s^{-1} in non-Faradaic potential window of (a) FeMo/NC-0.005, (b) FeMo/NC-0.01 and (c) FeMo/NC-0.02.

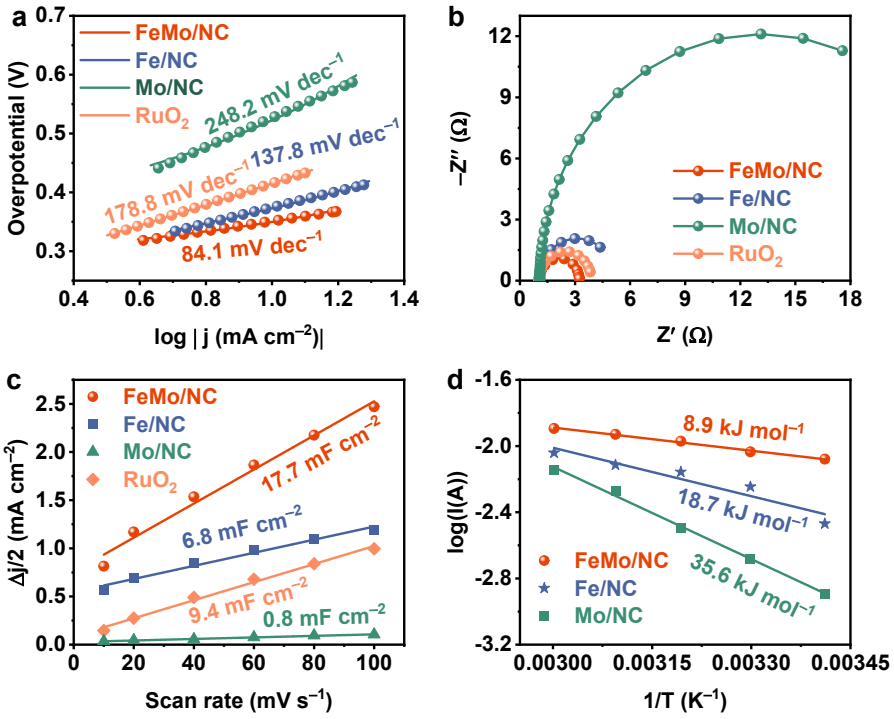

Fig. S12. Electrochemical OER performance of FeMo/NC, Fe/NC, Mo/NC and RuO_2. (a) Tafel slope. (b) Nyquist plots. (c) Electrochemical double-layer capacitance. (d) Arrhenius plots of kinetics current.

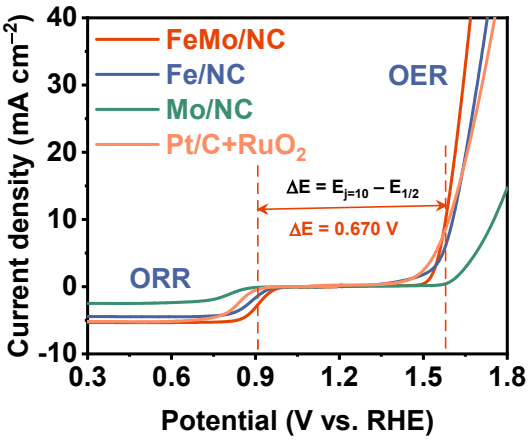

Fig. S13. The potential difference (ΔE) values of FeMo/NC, Fe/NC, Mo/NC and Pt/C.

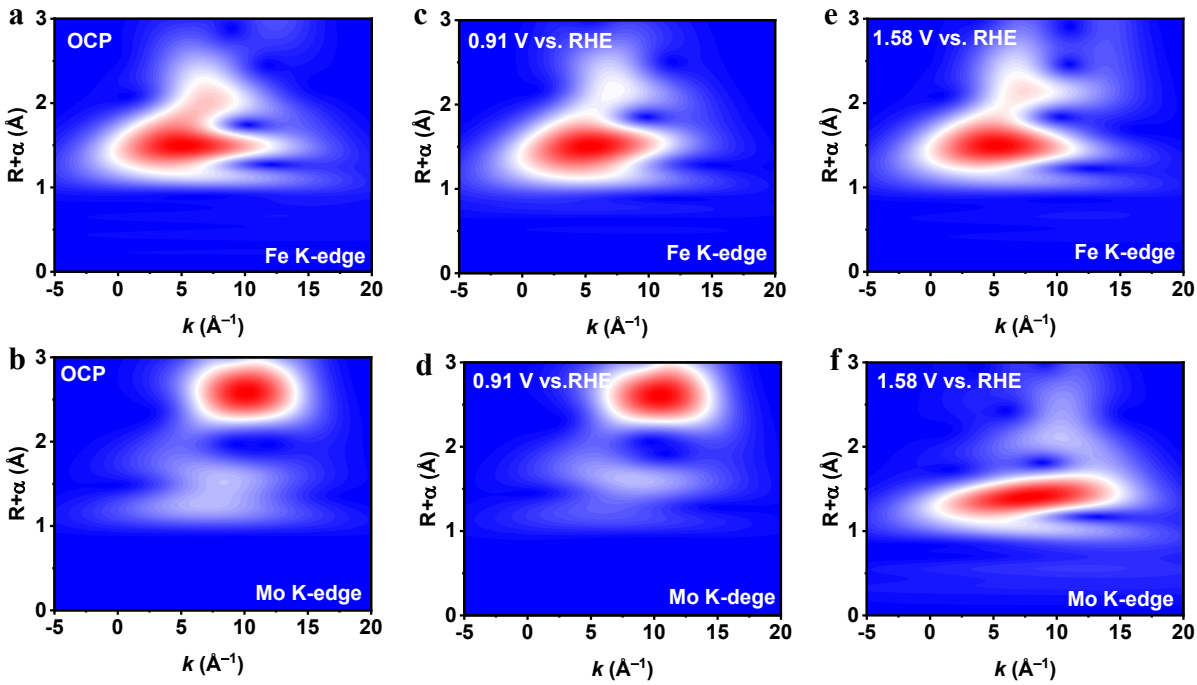

Fig. S14. Fe and Mo K-edge WT-EXAFS spectra for FeMo/NC (a-b) at OCP, (c-d) 0.91V vs. RHE and (e-f) 1.58 V vs. RHE.

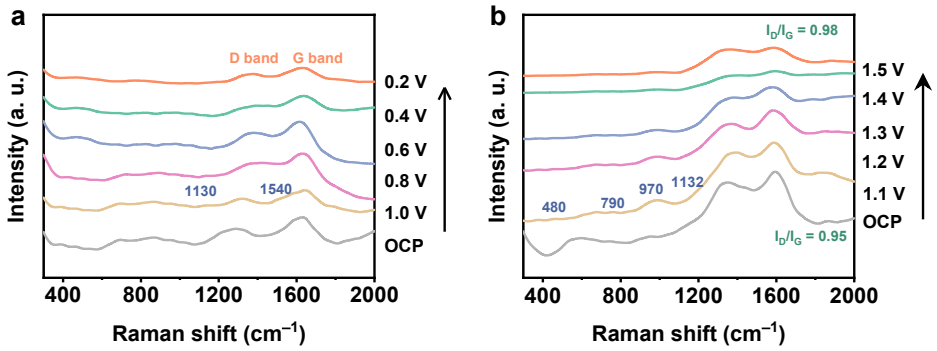

Fig. S15. *In situ* Raman spectra of FeMo/NC for (a) ORR and (b) OER.

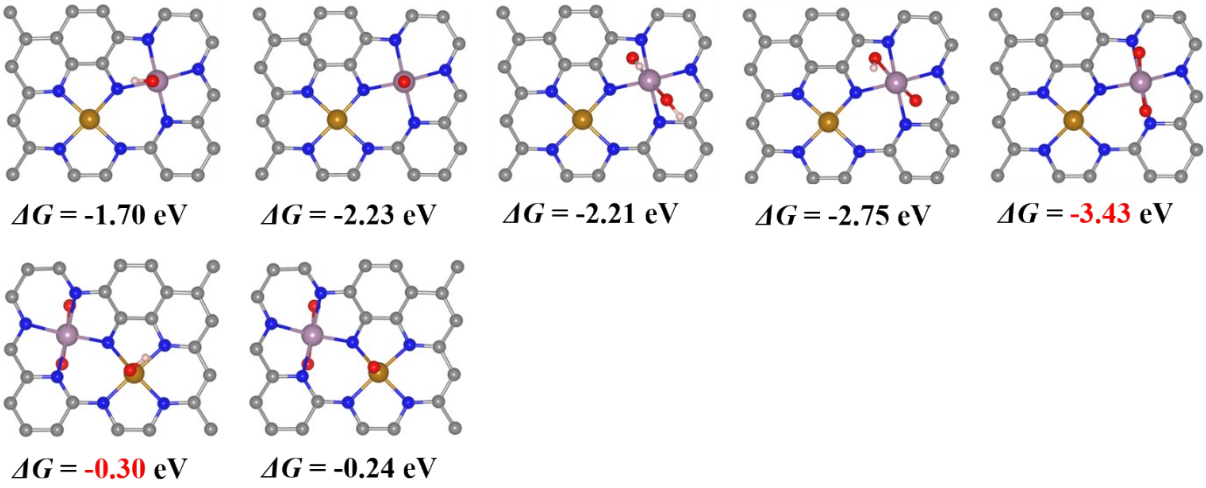

Fig. S16. Stability and atomic structures of FeMo/NC with adsorbed OH and O species under ORR operating conditions.

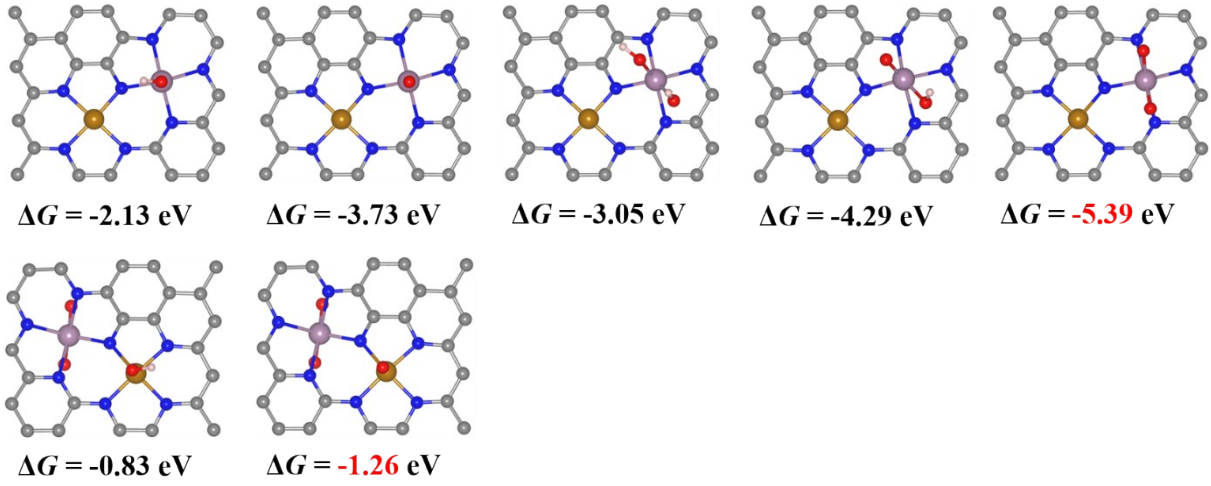

Fig. S17. Stability and atomic structures of FeMo/NC with adsorbed OH and O species under OER operating conditions.

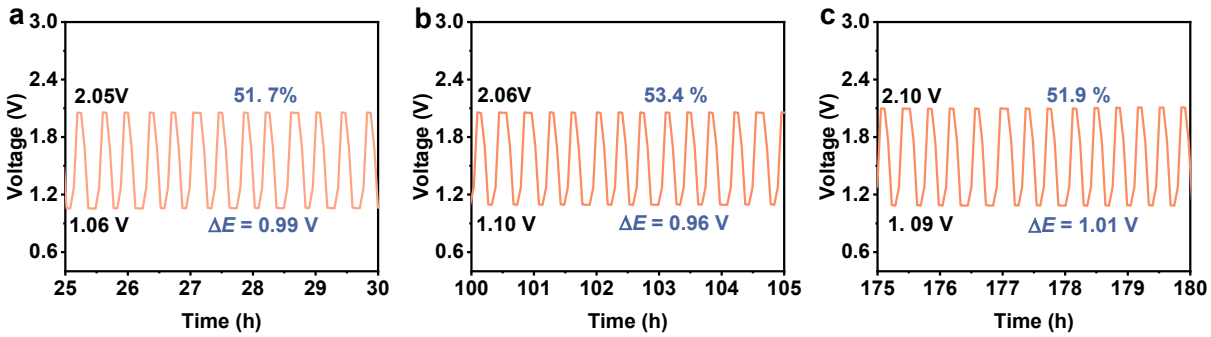

Fig. S18. Energy efficiency and voltage gap of FeMo/NC-based LZAB at the beginning, middle, and end of stability testing.

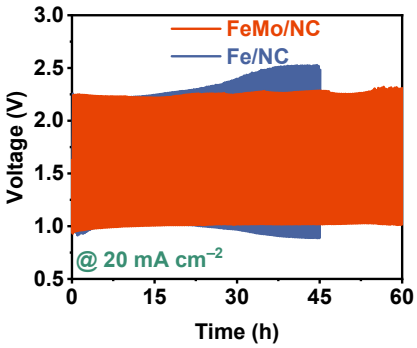

Fig. S19. Stability tests of FeMo/NC-based LZAB and Fe/NC-based LZAB at 20 mA cm^{-2}.

Table S1. Curve fit parameters of Fe K edge and Mo edge EXAFS for FeMo/NC

Sample[a]	Path	R/Å[c]	N[b]	σ^2 (10^{-3}Å^2)[d]	ΔE_0/eV	R-factor
FeMo/NC	Fe-N	1.980±0.016	3.80±0.18	0.005	9.60±1.45	0.004
	Fe-Mo	3.698±0.015	1.00±0.13	0.007	9.50±1.60	0.004
	Mo-N	2.100±0.012	4.20±0.20	0.007	9.40±1.55	0.003
	Mo-Fe	3.704±0.017	1.20±0.17	0.008	9.55±1.58	0.003

[a] S_0^2 was fixed as 0.9. [b] N is the coordination number. [c] R is the distance between absorber and backscatter atoms. [d] σ^2 is the Debye-Waller factor. R-factor is residual factor.

Table S2. Comparison of the ORR performance of DACs in 0.1 M KOH

Catalysts	$E_{1/2}$ (V)	Tafel (mV dec^{-1})	References
FeMo/NC	**0.91**	**53.8**	**This work**
FeN_4B-NiN_4B	0.9	61	[19]
Fe_2@P-HC	0.89 V	97	[20]
FeCu-NC	0.882	74	[21]
(Zn, Cu)–NC	0.88	87.1	[22]
Fe-Co-NC	0.88	54.8	[23]
NiN_4–Fe_5–FeN_4@PCF	0.878	95.9	[24]
FeNi-NPC-1000	0.877	69.11	[25]
Co, Fe-DACs/NCs@PCF	0.871	75	[26]
Co_2-DAs@CHNSs	0.87	80	[27]
HP/FeCo-NC-2	0.865	95.27	[28]
FeN_3-CuN_3	0.85	120.7	[29]
FeMn/NC	0.85	65	[30]
Fe-NiNC-50	0.84	55	[31]

Table S3. Comparison of bifunctional properties of DACs in alkaline electrolytes

Catalysts	$E_{1/2}$ (V vs. RHE)	$E_{j=10}$ (V vs. RHE)	ΔE (V vs. RHE)	Reference
FeMo/NC	0.91 (0.1 M KOH)	1.58 (1.0 M KOH)	0.67	**This work**
NCAG/Fe-Cu	0.94 (0.1 M KOH)	1.61 (1.0 M KOH)	0.67	[32]
Fe_2N_6-S	0.921 (0.1 M KOH)	1.60 (1.0 M KOH)	0.679	[33]
CoFe−N−C	0.897 (0.1 M KOH)	1.59 (1.0 M KOH)	0.693	[34]
FeMn-N/S-C	0.924 (0.1 M KOH)	1.617 (0.1 M KOH)	0.693	[35]
Co_2-N-HCS-900	0.86 (0.1 M KOH)	1.563 (1.0 M KOH)	0.703	[36]
FeCu-NC	0.85 (0.1 M KOH)	1.558 (1.0 M KOH)	0.708	[29]
Co, Fe-DACs/NCs@PCF	0.871 (0.1 M KOH)	1.588 (0.1 M KOH)	0.717	[26]
FeN_4B-NiN_4B	0.90 (0.1 M KOH)	1.618 (0.1 M KOH)	0.718	[19]
Fe–NiNC-50	0.84	1.57	0.73	[31]

	(0.1 M KOH)	(1.0 M KOH)		
NiN_4–Fe_5–FeN_4@PCF	0.878 (0.1 M KOH)	1.626 (0.1 M KOH)	0.748	[24]
CoNi-SAs/NC	0.76 (0.1 M KOH)	1.57 (1.0 M KOH)	0.81	[37]
Fe/Ni-DA-CNFs	0.79 (0.1 M KOH)	1.67 (0.1 M KOH)	0.88	[38]

Table S4. Curve fit parameters of Fe K-edge and Mo K-edge EXAFS for FeMo/NC at OCP, 0.91 V vs. RHE and 1.58 V vs. RHE

Sample[a]	Path	R/Å[c]	N[b]	σ^2 (10^{-3}Å^2)[d]	ΔE_0/eV	R-factor
OCP	Fe-N	2.020±0.015	3.90±0.14	0.006	9.95±1.34	0.003
	Fe-O	2.587±0.018	0.90±0.12	0.007	9.85±1.45	0.004
	Fe-Mo	3.713±0.017	1.10±0.15	0.007	9.78±1.20	0.004
	Mo-N	2.132±0.014	4.30±0.18	0.006	9.54±1.31	0.003
	Mo-O	2.882±0.012	0.90±0.19	0.006	9.82±1.30	0.003
	Mo-Fe	3.727±0.010	1.3±0.10	0.007	9.71±1.25	0.002
0.91 V vs. RHE	Fe-N	1.994±0.018	4.00±0.11	0.007	9.20±1.33	0.002
	Fe-O	2.550±0.016	0.90±0.20	0.007	9.76±1.27	0.002
	Fe-Mo	3.693±0.014	1.10±0.23	0.008	9.80±1.23	0.004
	Mo-N	2.105±0.012	4.30±0.21	0.007	9.65±1.28	0.004
	Mo-O	2.887±0.010	1.10±0.25	0.007	9.40±1.25	0.004
	Mo-Fe	3.712±0.008	1.34±0.16	0.006	9.27±1.20	0.003
1.58 V vs. RHE	Fe-N	1.967±0.016	4.10±0.26	0.007	9.45±1.32	0.002
	Fe-O	2.517±0.013	1.00±0.22	0.007	9.20±1.25	0.002
	Fe-Mo	3.695±0.014	1.20±0.19	0.008	9.75±1.40	0.003

	Mo-N	1.975±0.010	4.40±0.15	0.007	9.70±1.28	0.004
	Mo-O	2.751±0.008	1.20±0.20	0.007	9.55±1.30	0.004
	Mo-Fe	3.693±0.016	1.30±0.17	0.006	9.40±1.35	0.003

[a] S_0^2 was fixed as 0.9. [b] N is the coordination number. [c] R is the distance between absorber and backscatter atoms. [d] σ^2 is the Debye-Waller factor. R-factor is residual factor.

Table S5. Comparison of the performance of DACs-based ZABs

Catalysts	Open-circuit voltage (V)	Peak power density (mW cm^{-2})	Specific capacity (mAh g_{Zn}^{-1})	References
FeMo/CN	**1.54**	**182**	**825.7**	**This work**
FeCu-NC	1.52	108.5	718.2	[29]
CoNi-SAs/NC	1.45	101.4	750.9	[37]
Fe-O_2-Fe	1.56	178	819	[39]
FeMn/NC	1.464	129	821.5	[30]
Co_2-DAs@CHNSs	1.47	130.52	787.14	[27]
(Zn, Cu)–NC	1.50	163.8	785.7	[22]
FeN_4-NiN_4	1.498	236.9	771.7	[19]
Co_2-N-HCS-900	1.45	188.2	754.2	[36]
NiN_4–Fe_5–FeN_4@PCF	1.58	N/A	781.8	[24]
CoFe−N−C	1.49	142.1	N/A	[34]
Fe–NiNC-50	1.41	220	752.14	[31]

References

1 G. Kresse, J. Furthmüller, *Phys. Rev. B*, 1996, **54**, 11169.

2 P.E. Blöchl, *Phys. Rev. B*, 1994, **50**, 17953-17979.

3 J.P. Perdew, J.A. Chevary, S.H. Vosko, K.A. Jackson, M.R. Pederson, D.J. Singh, C. Fiolhais, *Physical Review B*, 1992, **46**, 6671-6687.

4 S. Grimme, J. Antony, S. Ehrlich, H. Krieg, *The Journal of Chemical Physics*, 2010, **132**, 154104.

5 H.J. Monkhorst, J.D. Pack, *Phys. Rev. B*, 1976, **13**, 5188-5192.

6 J.K. Nørskov, J. Rossmeisl, A. Logadottir, L. Lindqvist, J.R. Kitchin, T. Bligaard, H. Jónsson, *J. Phys. Chem. B*, 2004, **108**, 17886-17892.

7 http://webbook.nist.gov/chemistry/.

8 K. Mathew, R. Sundararaman, K. Letchworth-Weaver, T.A. Arias, R.G. Hennig, *J. Chem. Phys.*, 2014, **140**, 084106.

9 Z. Duan, P. Xiao, *J. Phys. Chem. C.*, 2021, **125**, 15243-15250.

10 Z. Duan, G. Henkelman, *J. Phys. Chem. C.*, 2020, **124**, 12016-12023.

11 Q. Liang, G. Brocks, A. Bieberle-Hütter, *J. Phys. Energy*, 2021, **3**, 026001.

12 H. Xu, D. Cheng, D. Cao, X.C. Zeng, *Nat. Catal.*, 2024, **7**, 207-218.

13 H.A. Hansen, J. Rossmeisl, J.K. Nørskov, *Phys. Chem. Chem. Phys.*, 2008, **10**, 3722-3730.

14 L. Qi, X. Bai, Y. Wang, Z. Duan, L. Li, J. Guan, *CCS Chem.*, 2025, **7**, 2508–2519.

15 S. Ran, J. Qi, X. Dong, H. Huang, M. Qi, W. Dong, P. Zhao, Z. Zhao, J. Yang, *Chem. Eng. J.*, 2023, **463**, 142174.

16 X. Bai, Y. Wang, J.Y. Han, X.D. Niu, J.Q. Guan, *Appl. Catal. B Environ. Energy*, 2023, **337**, 122966.

17 C. Hu, Q. Liang, Y. Yang, Q. Peng, Z. Luo, J. Dong, T.T. Isimjan, X. Yang, *J. Colloid Interface Sci.*, 2023, **633**, 500-510.

18 L. Wang, J. Huang, X. Hu, Z. Huang, M. Gao, D. Yao, T. Taylor Isimjan, X. Yang, *J. Colloid Interface Sci.*, 2024, **660**, 989-996.

19 Z. Wang, R. Xu, Q. Ye, X. Jin, Z. Lu, Z. Yang, Y. Wang, T. Yan, Y. Liu, Z. Pan, S.J. Hwang, H.J. Fan, *Adv. Funct. Mater.*, 2024, **34**, 2315376.

20 Q. Miao, Z. Chen, X. Li, M. Liu, G. Liu, X. Yang, Z. Guo, C. Yu, Q. Xu, G. Zeng, *ACS Catal.*, 2023, **13**, 11127-11135.

21 Z. Xiao, P. Sun, Z. Qiao, K. Qiao, H. Xu, S. Wang, D. Cao, *Chem. Eng. J.*, 2022, **446**, 137112.

22 D. Deng, J. Qian, X. Liu, H. Li, D. Su, H. Li, H. Li, L. Xu, *Adv. Funct. Mater.*, 2022, **32**, 2203471.

23 L. Wu, Y. Chen, C. Shao, L. Wang, B. Li, *Adv. Funct. Mater.*, 2024, **34**, 2408257

24 R. Xu, Z. Wang, X. Jin, T. Li, Z. Lu, Z. Yang, K. Kong, Y. Zhang, Y. Wang, Y. Liu, Z. Pan, S.-J. Hwang, J. Fang, *J. Colloid Interface Sci.*, 2025, **693**, 137620.

25 Y. He, J. Yang, Y. Wang, Y. Jia, H. Li, Y. Liu, L. Liu, Q. Tan, *ACS Appl. Mater. Interfaces*, 2024, **16**, 12398-12406.

26 Z. Lu, Z. Wang, Z. Yang, X. Jin, L. Tong, R. Xu, K. Kong, Y. Zhang, Y. Wang, Y. Liu, L. Meng, Z. Pan, S.J. Hwang, L. Li, *Adv. Funct. Mater.*, 2024, **35**, 2418489.

27 T. Lu, Q. Zhou, J. Li, T. Li, J. Gong, S. Zhang, H. Pang, S. Xi, L. Xu, G. Luo, D. Sun, K. Sun, Y. Tang, *Adv. Funct. Mater.*, 2024, **34**, 2405564.

28 J. Guo, Q. An, Y. Zhang, J. Zhang, B. Li, S. Bo, J. Jiang, W. Wang, Q. Liu, *The Journal of Physical Chemistry C*, 2024, **128**, 9454-9461.

29 Y. Zhang, B. Yan, C. Ji, T. Wei, W. Niu, H. Lin, Y. Shi, *Chem. Eng. J.*, 2024, **500**, 157182.

30 X. Sheng, Z. Mei, Q. Jing, X. Zou, L. Wang, Q. Xu, L. Yang, H. Guo, *ACS Sustainable Chem. Eng.*, 2023, **11**, 7263-7273.

31 X. Zhu, D. Zhang, C.-J. Chen, Q. Zhang, R.-S. Liu, Z. Xia, L. Dai, R. Amal, X. Lu, *Nano Energy*, 2020, **71**, 104597.

32 T. He, Y. Chen, Q. Liu, B. Lu, X. Song, H. Liu, M. Liu, Y.N. Liu, Y. Zhang, X. Ouyang, S. Chen, *Angew. Chem. Int. Ed.*, 2022, **61**, e202201007.

33 M. Liu, X. Wang, S. Cao, X. Lu, W. Li, N. Li, X.H. Bu, *Adv. Mater.*, 2024, **36**, 2309231.

34 X. Zhou, J. Gao, Y. Hu, Z. Jin, K. Hu, K.M. Reddy, Q. Yuan, X. Lin, H.-J. Qiu, *Nano Lett.*, 2022, **22**, 3392-3399.

35 Y. He, H. Li, Y. Wang, Y. Jia, Y. Liu, Q. Tan, *J. Energy Chem.*, 2024, **90**, 610-620.

36 X. Wang, L. Xu, C. Li, C. Zhang, H. Yao, R. Xu, P. Cui, X. Zheng, M. Gu, J. Lee, H.

Jiang, M. Huang, *Nat. Commun.*, 2023, **14**, 7210.

37 X. Han, X. Ling, D. Yu, D. Xie, L. Li, S. Peng, C. Zhong, N. Zhao, Y. Deng, W. Hu, *Adv. Mater.*, 2019, **31**, 1905622.

38 Y. Zheng, G. Zhu, G. Li, H. Guo, Z. Li, X. Han, J. Li, L. Dong, J. Zang, Y. Wang, *Diamond Relat. Mater.*, 2024, **142**, 110761.

39 X. Xu, T. Gan, J. Guan, *CCS Chem.*, 2025, https://doi.org/10.31635/ccschem.31025.202505566.